

Chapter One

The Lyman- α Line as a Probe of the Early Universe

1.1 LYMAN- α EMISSION FROM GALAXIES

We saw in §?? that young star-forming can produce very bright Lyman- α emission; indeed searching for bright line Lyman- α line emitters is one of the most effective ways to find high- z galaxies. Although the radiative transfer of these photons through their host galaxies is typically very complex, a good starting point is a simple model in which a fraction of stellar ionizing photons are absorbed within their source galaxy; the resulting protons and electrons then recombine, producing Lyman- α photons. Assuming ionization equilibrium, the rate of these recombinations must equal the rate at which ionizing photons are produced. However, direct recombinations to the ground state (which occur $\approx 1/3$ of the time, from the ratio of the case-A and case-B recombination coefficients α_A and α_B) simply regenerate the initial ionizing photon, so they do not contribute to the net balance.

Because only hot, massive stars – which live for only several million years – produce ionizing photons, it is a good approximation to assume that the rate at which any given galaxy generates these photons is proportional to its instantaneous star formation rate \dot{M}_* . The proportionality constant, which we will call $N_{\text{Ly}\alpha}$, depends on the initial mass function (IMF) of stars, because that determines what fraction of stellar mass enters these massive, hot stars. For example, a Salpeter IMF with a metallicity $Z = 0.05Z_\odot$ produces¹ $N_\gamma = 3 \times 10^{53}$ ionizing photons per second per $M_\odot \text{ yr}^{-1}$ in stars formed. However, a top-heavy Population III IMF produces more than an order of magnitude more ionizing photons.

Finally, if we assume as usual that f_{esc} of the ionizing photons escape their host galaxy, then the intrinsic line luminosity of a galaxy is

$$L_{\text{Ly}\alpha}^{\text{int}} = \frac{2}{3} N_\gamma h\nu_\alpha (1 - f_{\text{esc}}) \dot{M}_*. \quad (1.1)$$

For context, a Salpeter IMF from 1 to 100 M_\odot with $Z = 0.05Z_\odot$ has a prefactor $3.8 \times 10^{42} (1 - f_{\text{esc}}) \text{ erg s}^{-1}$, if the star formation rate is measured in $M_\odot \text{ yr}^{-1}$.

Unfortunately, inferring physical properties about distant galaxies from the Lyman- α line is complicated not only by the uncertain factors f_{esc} and N_γ but also by the radiative transfer of these line photons through the interstellar and circum-galactic medium surrounding each galaxy. Because the Lyman- α line is so optically thick in both the galaxy's ISM and the nearby IGM, these photons scatter many times before they can escape the galaxy, and once they leave it they can be scattered away from the line of sight and vanish. This scattering can change not only the overall

brightness of the line but also its frequency structure and relation to the galaxy's continuum photons. The *observed* line luminosity is then

$$L_{\text{Ly}\alpha}^{\text{int}} = \frac{2}{3} T_{\text{Ly}\alpha}^{\text{IGM}} T_{\text{Ly}\alpha}^{\text{ISM}} N_{\gamma} h \nu_{\alpha} (1 - f_{\text{esc}}) \dot{M}_{\star}, \quad (1.2)$$

where $T_{\text{Ly}\alpha}^{\text{ISM}}$ is the fraction of Lyman- α photons that are transmitted through the galaxy's ISM and $T_{\text{Ly}\alpha}^{\text{IGM}}$ is the fraction that are transmitted through the IGM.

1.1.1 Radiative Transfer of Lyman- α Photons Through the Interstellar Medium

We will first consider radiative transfer within the galaxy and its immediate environs; we will defer discussion of IGM scattering until §???. The important difference from continuum transfer is that line photons can scatter many times (changing both their direction and frequency) as they traverse the ISM. In the case of Lyman- α photons, scattering cannot destroy them (because there are no other transitions through which the excited atom can decay), but dust absorption can. Depending on the geometry of the ISM, the increased path length can increase or decrease the brightness of the line relative to the continuum.

Some simple toy models of radiative transfer help to develop some intuition for this situation. We assume that the absorption cross-section follows the usual Voigt profile, $\sigma_{\alpha}(x) = \sigma_0 \phi_V(x)$. Here $x = (\nu - \nu_{\alpha})/\nu_D$ is the normalized frequency, with a Doppler broadening $\nu_D/\nu_{\alpha} = \sqrt{2k_B T/m_p c^2}$. The Voigt profile includes Gaussian thermal broadening in the core and natural Lorentzian broadening in the wings (usually referred to as the ‘‘damping wing’’); in that limit $\sigma_{\alpha} \approx a/(\sqrt{\pi}x^2)$ where $a = \nu_L/(2\nu_D) = 4.72 \times 10^{-4} T_4^{-1/2}$, $T_4 = T/(10^4 \text{ K})$, and $\nu_L = 4.03 \times 10^{-8}$ is the natural width of the line. Figure 1.1 shows the absorption cross-section for absorbing gas with $T = 10^4 \text{ K}$; note the gaussian core with width $\sim 10 \text{ km s}^{-1}$ and the much weaker, but broader, damping wings.

- *Homogeneous H I slab, moderately optically thick:* First consider a Lyman- α photon produced inside a homogeneous medium of pure H I, with total line-center optical depth $\tau_0 \gg 1$; note that, because τ_0 is proportional to distance in the medium, we can use it as a proxy for physical location within the system. So long as the photon remains in the Doppler core of the line, it barely diffuses spatially before being scattered by an atom. When a line photon of frequency x_{in} is absorbed by an atom, it re-emits a line photon of the same frequency in its own rest frame. However, in an observer's frame there will be a net frequency shift determined by the Lorentz transformation between the frames. To linear order, this is

$$x_{\text{out}} \approx x_{\text{in}} - \frac{\mathbf{v}_a \cdot \mathbf{k}_{\text{in}}}{v_{\text{th}}} + \frac{\mathbf{v}_a \cdot \mathbf{k}_{\text{out}}}{v_{\text{th}}} + g(\mathbf{k}_{\text{in}} \cdot \mathbf{k}_{\text{out}} - 1), \quad (1.3)$$

where \mathbf{v}_a is the velocity vector of the atom, $v_{\text{th}} = (2k_B T/m_p)^{1/2}$ is the thermal velocity of the gas, and \mathbf{k}_{in} and \mathbf{k}_{out} are the propagation directions of the incoming and outgoing photons, respectively. The last term g represents recoil; it is unimportant here, but we will revisit it in §??. Typically, the

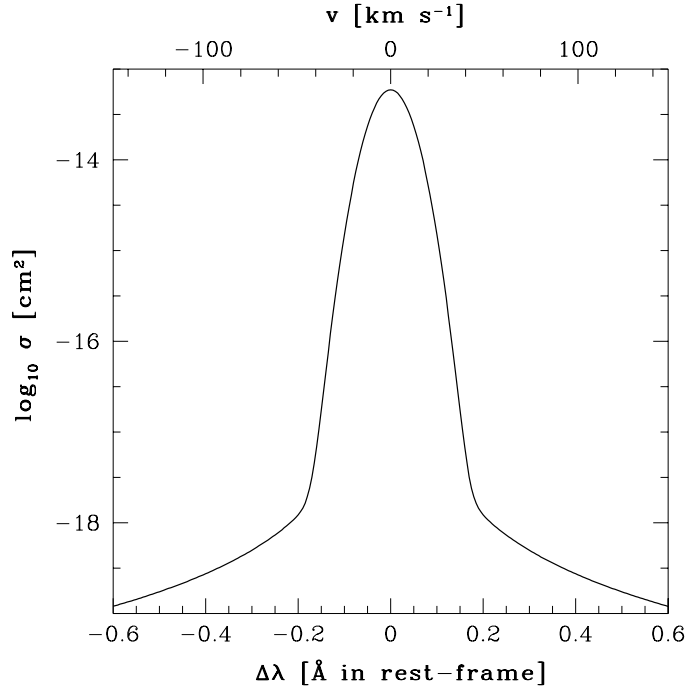


Figure 1.1 Cross-section for Lyman- α absorption, as a function of wavelength offset from line center (bottom axis) or velocity difference (top axis). We assume Voigt profile absorption generated by gas with $T = 10^4$ K. Figure credit: Santos, M.R. 2004, MNRAS, 349, 1137.

scattering atom will have the same velocity along the photon's direction of motion as the atom that emitted it, but it can have a much larger total velocity. In that case, the scattered photon will be far from line center.

If the medium is not too optically thick, so that the damping wings are themselves optically thin, the resulting photon can escape so long as it is produced at a frequency where $\tau(x) < 1$; for $\tau_0 = 10^3$, this corresponds to $x \sim 2.6$. We therefore generically expect that the resulting emission will have a double-peaked profile: photons near line-center do not escape; only when they diffuse to large positive or negative velocity are they able to escape. The Lyman- α surface brightness will also be compact, because photons escape after a single scattering.

- *Homogeneous HI slab, very optically thick:* In a moderately optically thick medium, these escaping photons simply result from rare scatterings off high-velocity atoms. If, on the other hand, the damping wings are optically thick, $\tau_0 a > 10^3$, so that once a photon is scattered into the wing the next scattering is more likely to be from interaction with an atom in the wings of its line than with an atom traveling at a matched velocity, the problem is more

complicated, though the net result is easy to understand: the photons must make it even farther into the wings to escape.

To do so, they must undergo a random walk of repeated scatterings, which occasionally take them far enough from line center to escape. Because scatterings usually occur in the core, each one induces an rms frequency shift $x \sim 1$, with a small bias $-1/x$ toward returning to line center; a photon thus typically undergoes $N_s \sim x^2$ scattering events before returning to line center. Between scatterings, the photon traverses a path length (in optical depth units) of $\tau\Phi(x) \sim 1$. Thus over its entire random walk, it diffuses a distance of $\tau_0^{\text{rms}} \sim \sqrt{N_s}\tau \sim |x|/\phi_V$. If this distance exceeds the size of the system (τ_0 in these units), the photon can escape. In the wings of the line where $\phi_V \sim a/x^2$, this requires that the photon have a critical normalized escape frequency

$$|x_{\text{esc}}| \sim (a\tau_0)^{1/3} \approx 30T_4^{-1/3}N_{21}^{1/3}, \quad (1.4)$$

where N_{21} is the column density of the system in units of 10^{21} cm^{-2} . Thus, in this highly-optically thick case, the photons must scatter far enough in the wings of the line to physically escape the system before scattering back to line center. This, combined with the power law form of ϕ_V in the wings, also makes the blue and red emission peaks wider than in the moderate optical depth case. The surface brightness of the line will be extended even if the source is compact, because photons diffuse spatially as well as in frequency before escaping.

- *Homogeneous H I slab, with velocity gradient:* We next consider a medium with a velocity gradient. Such a gradient can either correspond to expansion, arising from winds (which we believe to be ubiquitous in the star-forming galaxies likely to host Lyman- α emission lines), or contraction, from the infall of surrounding material around the galaxy.

First consider an expanding medium. Then, according to equation (1.3), scattered photons typically obtain a redshift: $\mathbf{v}_a \cdot \mathbf{k}_{\text{in}}$ is positive for photons propagating outward, while $\langle \mathbf{v}_a \cdot \mathbf{k}_{\text{out}} \rangle = 0$, so $x_{\text{out}} < x_{\text{in}}$ on average. Photons with $x < 0$ are therefore moved farther into the line wings, facilitating their escape, while photons with $x > 0$ are moved back toward line center. So long as the expansion velocity is much larger than the thermal velocities, this will prevent photons that experience large positive frequency jumps from escaping. Thus we expect only a single emission line, on the red side. In contrast, in a contracting medium photons typically obtain a blueshift, producing a single emission line on the blue side.

In this case the frequency shift of the surviving line depends upon the velocity and density structure of the medium. The case of most practical relevance is a wind, in which a large column of H I occurs at $\pm v_{\text{wind}}$ along the line of sight, with negligible absorption elsewhere. In this case photons that begin their escape toward the observer (i.e., through the blueshifted wind) are absorbed. After their first scattering, photons that begin their escape toward the far

component of the wind lie to the red side of the line. Those that scatter back toward the observer are then far to the red of the (blueshifted) wind and can continue to the observer. The observed velocity offset is then v_{wind} and provides a good diagnostic of the wind.

- *Homogeneous H I slab with dust:* Now we can add dust to a (static) medium and see how it can destroy the Lyman- α photons. We let the *total* dust interaction cross-section, per hydrogen nucleus, be σ_d ; this includes both absorption, with a cross-section $\sigma_a = \epsilon_a \sigma_d = \sigma_{a,21}/(10^{-21} \text{ cm}^2/\text{H})$, and scattering. For the well-studied dust in the Milky Way, $\sigma_{a,21} \approx 1$ and $\epsilon_a \approx 0.5$. The average absorption probability per interaction (with either dust or H I) is therefore

$$\epsilon = \frac{\sigma_a}{x_{\text{HI}}\phi_V(x)\sigma_0 + \sigma_d} \approx \frac{\beta}{\phi_V(x)}, \quad (1.5)$$

where $\beta = \sigma_a/(x_{\text{HI}}\phi_V = 1.69 \times 10^{-8} T_4^{1/2} \sigma_{a,21}/x_{\text{HI}}$ and we have assumed that dust interactions are rare compared to H I scattering.

Now recall that, in order to escape the H I, the photon must first scatter far into the wings of the line and then stay in the wings as it spatially diffuses out of the system. During that process, the photon will scatter N_s times; the probability that it is absorbed is therefore $P_{\text{abs}} \sim N_s \epsilon \sim x^4 \beta/a$ in the damping wing. This is near unity if $|x| > x_{\text{abs}}$, where

$$x_{\text{abs}} \sim (a/\beta)^{1/4} \sim 12.9 \left(\frac{x_{\text{HI}}}{T_4 \sigma_{a,21}} \right)^{1/4}. \quad (1.6)$$

A typical photon will therefore be unable to escape if $x_{\text{esc}} > x_{\text{abs}}$; if the line center optical depth exceeds a critical value $\tau_c \sim (a\beta^3)^{1/4}$, the emission line will be strongly suppressed. This corresponds to a column density of only $N_{21,c} = 0.08 T_4^{1/4} (x_{\text{HI}}/\sigma_{a,21})^{3/4}$, well below the typical column densities of galaxies (which are comparable to DLAs). Thus Lyman- α absorption can be very important inside the ISM. In general, in a uniform medium the line photons are more affected by dust than continuum photons, because the many scatterings they suffer forces them to have a much longer path length than continuum photons, providing a much larger opportunity for dust absorption.

- *Multiphase medium with dust:* Finally, we consider a medium in which both the H I and dust are confined to optically thick, discrete clouds separated by a highly-ionized, dust-free “inter-cloud medium.” Here the results will clearly depend on the geometry of the system, but some general considerations do apply. First, note that an inhomogeneous medium will allow *more* transmission than a homogeneous slab with identical column density of neutral gas, because of the same arguments we saw for IGM transmission in an inhomogeneous IGM (see §??). Moreover, the line photons can be *less* affected by dust than continuum photons, because the line photons scatter off the *surface* of the clouds, while the continuum photons plow through them and can encounter *more* dust.

Detailed calculations show that the frequency shift necessary for dust absorption to dominate over resonant scattering in the line wings, x_{abs} , is similar in magnitude to the homogeneous case. However, dust was so important in that example because Lyman- α photons *needed* to diffuse in frequency in order to escape the medium. This is not the case for a multiphase medium. In this case, photons enter each cloud on their surface and suffer relatively few scattering events inside each cloud before spatially diffusing back out. They can then travel a large distance before hitting another cloud, and spatial diffusion through the inter-cloud medium provides most of the impetus toward escape. Thus dust absorption will be relatively weak provided that the typical frequency shift before escape is less than x_{abs} .

In this case, photons obtain frequency shifts both from the thermal motions of the scattering atoms and from the velocity dispersion between the absorbing clouds; if the latter is large (as would be the case if most of the dust were buried in dense molecular clouds), it dominates the frequency diffusion, because – just as for a wind – each cloud is so optically thick that in the observer’s frame the photon leaves each cloud with a velocity offset corresponding to that cloud’s velocity. If the clouds have a large velocity dispersion, then dust absorption within each cloud will dominate over resonant scattering, because the photons will enter each cloud in the wings of the line.

Although each of these toy models is obviously much simpler than a real galaxy, together they illustrate the complexity of the radiative transfer problem and the many parameters that can dramatically affect the Lyman- α line’s amplitude and shape, as well as the surface brightness of a line emitter. In general, even discounting uncertainties from IGM transmission discussed below, the Lyman- α line is therefore typically very difficult to interpret and is not regarded as, for example, a very reliable measure of the star formation rate. However, its brightness in many galaxies makes it such a useful signpost that it is still the subject of intense study.

1.1.2 Other Emission Lines

Because it can be such a bright line, and because its ultraviolet rest wavelength redshifts it into the optical or near-infrared in distant galaxies, the Lyman- α line gets the lion’s share of attention. But other emission lines can be as or even more useful for certain diagnostics, and we briefly mention them here. This is of course a very large and deep subject, so we refer the interested reader to the literature and other textbooks for more information (see the Appendix).

1. *Other hydrogen lines:* The other Lyman-series lines are almost never visible in high-redshift galaxies; after several scatterings, these photons are “recycled” via radiative cascades into either Lyman- α photons or a pair of photons from the forbidden $2s \rightarrow 1s$ decay (see §??). However, Balmer-series photons (and those beginning at even higher levels) are very useful diagnostics. They are initially generated through the same process as Lyman- α – recombinations following ionizations near hot, massive stars – but because such

photons can only interact with atoms already in the $n = 2$ state, they are not subject to scattering in the interstellar medium and escape galaxies relatively easily (especially since they have relatively long wavelengths and so are less subject to dust absorption, e.g., the $H\alpha$ line lies at 6563 \AA). They therefore offer much more robust measures of star formation rates, subject only to the (admittedly still substantial) uncertainty in the IMF.

Unfortunately, although $H\alpha$ and its cousins are extremely important for low-redshift galaxies, its relatively red rest wavelength has so far limited its usefulness for their high-redshift cousins.

2. *Helium lines:* He II has the same electronic structure as H I, but shifted to four times larger energies. As a result, its ionization potential is well beyond the cutoff of most stars – only rare Wolf-Rayet stars (i.e., massive stars undergoing rapid mass loss) and the most massive Population III stars are hot enough to significantly ionize it. He II Balmer- α photons (with a rest wavelength of 1640 \AA) are therefore the most promising diagnostic of such massive stars: they are produced through recombination cascades following the ionization of He II. Like $H\alpha$ photons, they are unaffected by resonant transfer, but as UV photons they are more subject to dust attenuation.
3. *Metal lines:* In nearby galaxies, many metal lines offer diagnostics of ISM characteristics like the density, metallicity, and temperature of the nebulae surrounding star-forming regions. As instruments improve, these will no doubt be just as useful for measurements of high- z galaxies, although (with most of the lines having rest wavelengths in the optical) they are less accessible for the more distant sources.

1.2 THE GUNN-PETERSON TROUGH

We now briefly discuss the fate of photons that begin their lives blueward of Lyman- α during the reionization era. These photons will redshift through the IGM; if they should pass through the Lyman- α resonance, they will experience substantial absorption from that gas. The scattering cross-section of the H I Lyman- α resonance line is given by equation (??), and we have already computed the total optical depth for a photon that redshifts through the Lyman- α resonance as it travels through the IGM (the so-called Gunn-Peterson optical depth in equation (??). The most important aspect of this calculation is the enormous overall optical depth in a fully-neutral IGM, $\tau_\alpha \sim 6.5 \times 10^5 x_{\text{HI}}$ at $z \sim 9$. Thus we expect that, before reionization, photons that redshift across the Lyman- α transition will be completely extinguished (and, indeed, the same will be true so far as the ionized fraction is $< 10^{-3}$).

However, not all photons will redshift through the resonance during the reionization era. Suppose that a photon is emitted by a source at a redshift z_s beyond the “redshift of reionization” z_{reion} , which for the purposes of this calculation is simply the last redshift along the particular line of sight of interest where $x_{\text{HI}} = 1$. (Note that this differs from the conventional definition of the end of reionization as the

moment of “overlap” between the ionized bubbles; the variations along different lines of sight can themselves contain interesting astrophysical information.) For simplicity we will further assume that $x_{\text{HI}} = 1$ for all $z > z_{\text{reion}}$. The corresponding scattering optical depth of a uniform, neutral IGM is a function of the observed wavelength λ_{obs} ,

$$\tau_{\alpha}(\lambda_{\text{obs}}) = \int_{z_{\text{reion}}}^{z_s} dz \frac{cdt}{dz} n_{\text{H},0} (1+z)^3 \sigma_{\alpha} [\nu_{\text{obs}}(1+z)]. \quad (1.7)$$

At wavelengths corresponding to the Lyman- α resonance between the source redshift and the reionization redshift, $(1+z_{\text{reion}})\lambda_{\alpha} \leq \lambda_{\text{obs}} \leq (1+z_s)\lambda_{\alpha}$, the optical depth is given by equation (1.7). Since $\tau_{\alpha} \sim 10^5$, the flux from the source is entirely suppressed in this regime. Similarly, the Lyman- β resonance produces another trough at wavelengths $(1+z_{\text{reion}})\lambda_{\beta} \leq \lambda \leq (1+z_s)\lambda_{\beta}$, where $\lambda_{\beta} = (27/32)\lambda_{\alpha} = 1026 \text{ \AA}$, and the same applies to the higher Lyman series lines. If $(1+z_s) \geq 1.18(1+z_{\text{reion}})$ then the Lyman- α and the Lyman- β resonances overlap and no flux is transmitted between the two troughs. The same holds for the higher Lyman-series resonances down to the Lyman limit wavelength of $\lambda_c = 912 \text{ \AA}$.

At wavelengths shorter than λ_c , the photons may be absorbed when they photoionize atoms of hydrogen or helium, even if they do not redshift into the Lyman series lines. The bound-free absorption cross-section of hydrogen is given by equation (1.10); the appropriate parameters for He II are given in §1.2 as well. A reasonable approximation to the total cross-section for a mixture of hydrogen and helium with cosmic abundances in the range of $54 < h\nu < 10^3 \text{ eV}$ is $\sigma_{\text{bf}} \approx \sigma_0(\nu/\nu_{\text{H},0})^{-3}$, where $\sigma_0 \approx 6 \times 10^{-17} \text{ cm}^2$. The redshift factor in the cross-section then cancels exactly the redshift evolution of the gas density and the resulting optical depth depends only on the elapsed cosmic time, $t(z_{\text{reion}}) - t(z_s)$. At high redshifts this yields,

$$\begin{aligned} \tau_{\text{bf}}(\lambda_{\text{obs}}) &= \int_{z_{\text{reion}}}^{z_s} dz \frac{cdt}{dz} n_0 (1+z)^3 \sigma_{\text{bf}} [\nu_{\text{obs}}(1+z)] \\ &\approx 1.5 \times 10^2 \left(\frac{\lambda}{100 \text{ \AA}} \right)^3 \left[\frac{1}{(1+z_{\text{reion}})^{3/2}} - \frac{1}{(1+z_s)^{3/2}} \right]. \quad (1.8) \end{aligned}$$

The bound-free optical depth only becomes of order unity in the extreme UV to soft X-rays, around $h\nu \sim 0.1 \text{ keV}$, a regime which is unfortunately difficult to observe due to absorption by the Milky Way galaxy.

Together, these effects imply very strong absorption of nearly all photons that begin blueward of $\lambda_{\alpha}(1+z_r)$, except for a recovery at very short wavelengths and the gaps between the Lyman-series troughs (though these will be blanketed by the Lyman- α and other forests just below z_{reion} , so even they will be extremely optically thick).

1.3 IGM SCATTERING IN THE BLUE WING OF THE LYMAN- α LINE

We now return to the fate of photons emitted within (or near) the Lyman- α line of a galaxy or quasar. In this case, the relative velocity and broadening of the line

from bulk, thermal, or turbulent motions is very significant, because it determines whether the photons pass through the Lyman- α resonance – and so experience the full Gunn-Peterson absorption – or remain redward of line center, experiencing much less absorption. We also must consider the environment of the source: whether it is embedded in completely neutral gas or in an ionized bubble, and the surrounding velocity field. In this section we will focus on photons emitted blueward of, but still near to, line center.

1.3.1 Resonant Scattering Inside Ionized Bubbles

Photons that begin slightly blueward of line center redshift into the Lyman- α resonance near to their source. In most models, this nearby region will already have been ionized, either by the source itself or by its neighbors (if it is part of a much larger ionized bubble). Thus it may seem that these photons will survive their journey through the IGM.

However, if we recall that $\tau_\alpha > 10^5 x_{\text{HI}}$ at these redshifts, it is immediately apparent that even in highly-ionized media the absorption can be substantial. In practice, the short mean free paths at high redshifts will most likely prevent the gas from becoming extremely ionized. We can estimate the residual ionized fraction inside the bubbles assuming ionization equilibrium and a uniform emissivity (or in other words that each bubble contains many sources). The equilibrium condition is then

$$\alpha_B n_H^2 = x_{\text{HI}} n_H \bar{\sigma}_{\text{HI}} (1+z)^2 \frac{3\dot{N}_\gamma}{4\pi R_b^2}, \quad (1.9)$$

where $\bar{\sigma}_{\text{HI}} \sim 2 \times 10^{-18} \text{ cm}^2$ is a frequency-averaged cross-section, \dot{N}_γ is the total rate of ionizing photon production inside the region, and λ is the comoving mean free path (either from LLSs or the finite bubble size). If we use our usual model for the ionizing sources, in which the rate of ionizing photon production is proportional to the rate at which gas accretes onto galaxies, we obtain (see eq. (??))

$$\dot{N}_\gamma = \zeta \dot{f}_{\text{coll}} \frac{4\pi}{3\bar{n}_H c \lambda^3}. \quad (1.10)$$

But we also know $Q_{\text{HII}} = \zeta \dot{f}_{\text{coll}} / (1 + \bar{n}_{\text{rec}})$, where \bar{n}_{rec} is the mean number of recombinations per atom. So we can rewrite the ionizing efficiency ζ in terms of the overall ionized fraction and solve for the resonant optical depth due to residual neutral gas x_{HI} inside the bubble:

$$\tau_\alpha^{\text{res}}(\delta) \approx 40 \frac{(1+\delta)^2}{Q_{\text{HII}}(1+\bar{n}_{\text{rec}})} \left(\frac{10 \text{ Mpc}}{\lambda} \right) \left(\frac{f_{\text{coll}}}{df_{\text{coll}}/dz} \right), \quad (1.11)$$

where we have assumed that the IGM is isothermal for the recombination coefficient. The factor involving the collapsed fraction is typically of order a few.

Clearly the optical depth for these photons is large in realistic models; note, however, that it is small enough that many of the radiative transfer effects important for photon escape from galaxies are not important, and the absorption from each gas parcel will not have a terribly broad width in frequency space.

1.3.2 The Proximity Effect and Quasar “Near-Zones”

We have now found that an average location inside an ionized bubble is not likely to be ionized strongly enough to allow significant transmission before reionization. However, the region immediately outside the of an ionizing source will be more ionized than average thanks to photons from that source. At moderate redshifts, this “proximity effect” is a useful measure of the ionizing background, and it is a very attractive probe of the reionization era as well.

The profile of the ionization rate around a quasar at moderate redshifts is simple to understand. Suppose that there is a (uniform) metagalactic background with amplitude Γ_{bg} . The central quasar, with luminosity L_ν , produces a specific intensity $J_\nu \propto L_\nu/R^2$, where R is the distance from the quasar. Thus we expect an ionization rate $\Gamma_q = \Gamma_{q,0}/R^2$. Assuming ionization equilibrium, we then have

$$\tau(R) \propto (\Gamma_{\text{bg}} + \Gamma_{q,0}/R^2)^{-1}. \quad (1.12)$$

A simple fit to the absorption profile as a function of distance from the quasar suffices to extract Γ_{bg} , especially if $\Gamma_{q,0}$ can be estimated from the observed luminosity of the quasar redward of the Lyman- α line. In practice, these estimates are complicated by variations in the Lyman- α forest lines themselves and by the biased environments of quasars: the quasar will only induce substantial changes in the radiation field within a small “proximity zone” around the quasar where $\Gamma_q > \Gamma_{\text{bg}}$. This corresponds to

$$R_{\text{prox}} = \frac{1.2\Gamma_{12}^{-1/2}}{\alpha + 3} \left(\frac{\nu L_\nu}{10^{44} \text{ erg s}^{-1}} \right)^{1/2} \text{ proper Mpc}, \quad (1.13)$$

where α is the quasar spectral index and L_ν is evaluated at the H I ionization edge. This places the proximity zone within the overdense environment of the quasar’s halo; the increased absorption from this excess gas partially cancels the effect of the increased ionizing background, making the proximity effect more difficult to see.

Because the ionizing background is much smaller during the reionization era, it may at first appear that the proximity effect will be easier to observe. However, in reality the effect is much more difficult to interpret because the IGM is so optically thick. In this situation, the observable pattern near a luminous source will be gradually increasing absorption until saturation is reached. Figure 1.2 shows some examples; the curves here have each been averaged over several independent lines of sight to reduce the scatter from the inhomogeneous IGM. Here the horizontal dotted line marks 10% transmission; this is conventionally used to mark the edge of the transmission region.

The key point is that, during the reionization era, there are two possible reasons why such saturation can occur. The first is if the source (usually a quasar) is still in the process of ionizing its neutral surroundings. Then there will be a sharp transition between the highly-ionized H II region and the nearly neutral gas at its edge, which will manifest itself as a dramatic increase in the local optical depth. The second is more similar to the classical proximity effect, except that the absorption may saturate long before the local ionization rate reaches the background value.

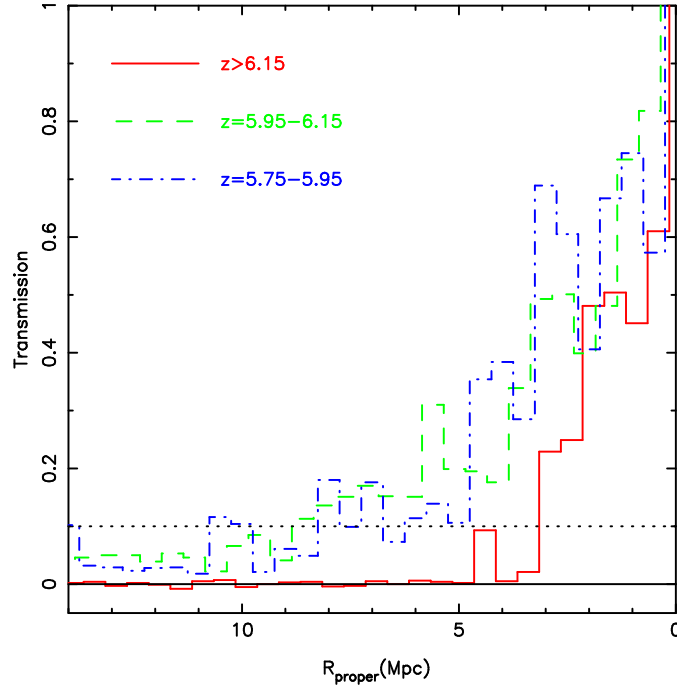


Figure 1.2 Average absorption profiles near the Lyman- α line for quasars in three different redshift bins. Note that the Lyman- α emission lines have been fitted and removed. The three redshift bins average over 8 ($5.75 < z < 5.95$), 9 ($5.95 < z < 6.15$), and 4 ($z > 6.15$) quasars. The horizontal dotted line marks 10% transmission, conventionally taken as the edge of the near-zone. Figure credit: Carilli, C.L. et al. 2010, ApJL, 714, 834.

Because the observed edge of the transmission does not necessarily correspond to the classical proximity zone, this feature is usually referred to as the “near-zone.”

In the first case, the size of the H II region depends on the ionizing luminosity of the quasar (which can be estimated from the spectrum redward of Lyman- α), the age of the quasar t_Q , and the average neutral fraction before the quasar appeared, \bar{x}_{HI} . The basic radiative transfer problem has already been solved in §??; for the purposes of a simple estimate, if recombinations can be neglected, the proper radius of the H II region is

$$R_b \approx \frac{4.2}{\bar{x}_{\text{HI}}^{1/3}} \left(\frac{\dot{N}}{2 \times 10^{57} \text{ s}^{-1}} \right)^{1/3} \left(\frac{t_Q}{10^7 \text{ yr}} \right)^{1/3} \left(\frac{1+z}{7} \right)^{-1} \text{ Mpc}, \quad (1.14)$$

where \dot{N}_Q is the rate at which the quasar produces ionizing photons and we have assumed that all the ionizing photons are absorbed but ignore secondary ionizations. Note that $R_b \propto (\dot{N}_Q t_Q / \bar{x}_{\text{HI}})^{1/3}$, varying relatively slowly with these parameters.

However, the absorption can become saturated well before this limit is reached. To estimate this, we suppose that the edge of the near-zone is where the transmis-

sion falls below T_{lim} , or the optical depth rises above τ_{lim} . We will take $T_{\text{lim}} = 0.1$ as a fiducial value (comparable to existing observations). Assuming that the background ionization rate can be neglected (likely a good assumption at these very high redshifts), the transmission reaches this limiting value at a proper radius

$$R_{\text{lim}} \approx 3.1 \left(\frac{\dot{N}}{2 \times 10^{57} \text{ s}^{-1}} \right)^{1/2} \left(\frac{T}{2 \times 10^4 \text{ K}} \right)^{0.38} \left(\frac{\tau_{\text{lim}}}{2.3} \right)^{1/2} \left[\frac{3\alpha}{(\alpha + 3)} \right]^{1/2} \left(\frac{1+z}{7} \right)^{-9/4}, \quad (1.15)$$

where the T dependence enters through the recombination coefficient for ionization equilibrium. Note that this limiting radius is independent of the neutral fraction of the material outside of the ionized zone, and it is slightly more sensitive to the quasar luminosity, $R_{\text{lim}} \propto \dot{N}_Q^{1/2}$.

However, equation (1.15) can only apply if the quasar bubble has reached that size. This requires

$$t_Q > 4.2 \times 10^6 \bar{x}_{\text{HI}} \left(\frac{R_{\text{lim}}}{3.1 \text{ Mpc}} \right)^3 \left(\frac{\dot{N}}{2 \times 10^{57} \text{ s}^{-1}} \right)^{-1} \left(\frac{1+z}{7} \right)^3 \text{ yr}. \quad (1.16)$$

(Adding recombinations and clumping will increase this scale by a factor of no more than a few.) Interestingly, this timescale is comparable to the canonical quasar lifetime $t_Q \sim 10^7$ yr in fully neutral gas, but for quasars positioned near the end of reionization (which are actually accessible to observations) this timescale is very short.

We therefore expect most quasar near-zones be limited by the proximity effect rather than the bubble size. If so, these zones can tell us little about the ionization state of the surrounding gas. In principle, this supposition can be tested by examining the luminosity dependence of the near-zone size, although the modest variation between the two models, and the large scatter intrinsic to any measurement in an inhomogeneous IGM, has made differentiating them difficult to date. Figure 1.3 shows the measured near-zone sizes for the current sample of quasars at $z > 5.75$. The left panel shows the trend with redshift (here all the near-zone sizes have been normalized to a common luminosity using the $R_b \propto \dot{N}_Q^{1/3}$ relation), while the right panel shows the dependence on absolute magnitude (with the mean trend with redshift removed).

In the right panel, the dotted curve shows $R_b \propto \dot{N}_Q^{1/3}$ (with arbitrary scaling); this is not a fit but is shown only for illustrative purposes. Clearly the large scatter in the near-zone sizes, even after a simple redshift correction, make it difficult to distinguish this behavior from that expected from the more classic proximity effect, $R_b \propto \dot{N}_Q^{1/2}$.

Nevertheless, there is clearly a steady increase in the near-zone size as redshift declines. One possible interpretation is a decrease in \bar{x}_{HI} with cosmic time; the data would require a decline by ~ 10 over the range $z = 6.4$ to $z = 5.8$. However, presuming that $z \sim 6$ is the tail end of reionization, the proximity effect is more likely to fix the near-zone size. In that case, the trend with redshift is most likely attributable to a rapid increase in the background ionization rate (by > 3 times), which can substantially boost the total ionization rate in the outskirts of the quasar's proximity zone.

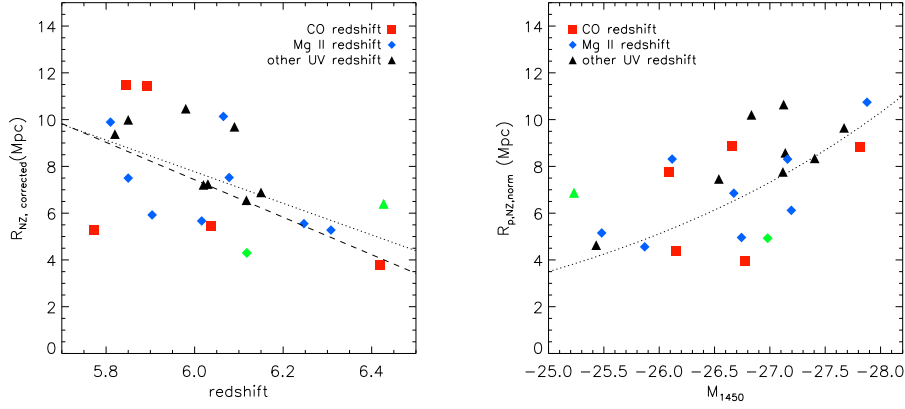


Figure 1.3 *Left*: Measured radii of near zones in a set of high- z quasars; the symbols denote the method used to compute the quasar’s redshift. All near-zone measurements have been scaled to a common quasar luminosity using the R_b relation in eq. (1.14) to better illustrate the trend with redshift. Typical errors in the near-zone size are ~ 1 Mpc. The two lines are fits to the trend with redshift. *Right*: Dependence of the near-zone size on quasar absolute magnitude; all the data points have been scaled to a common redshift using the mean relation in the left-hand panel to better illustrate the behavior with luminosity. The dotted line shows $R_b \propto \dot{N}_Q^{1/3}$ with arbitrary scaling; note that it is not a fit but is merely meant to guide the eye. Figure credit: Carilli, C.L. et al. 2010, ApJL, 714, 834.

Currently, the most challenging aspect of this measurement – other than finding these quasars in the first place – is determining the quasar’s location. The only tools we have are the redshifts of the source’s emission lines. Unfortunately, most quasars have strong internal motions and winds, which displaces many of the emission lines from the systemic redshift of the host. The best choices are low-excitation lines (such as Mg II) or, even better, lines from the host galaxy itself. Any such lines in the optical or UV are overwhelmed by the quasar’s own emission, so the most useful lines turn out to be those of CO, which are strong in these rapidly star-forming galaxies.

There is one additional, and very attractive, way to differentiate these two cases: by examining the absorption in higher Lyman-series lines. Because R_{lim} depends on the maximum detectable optical depth $\tau_{\text{lim}}^{1/2}$, it will increase by the square root of the optical depth ratio between the two lines; for Lyman- β , this means $R_{\text{lim}}^\beta \approx 2.5 R_{\text{lim}}^\alpha$. However, at the edge of the ionized bubble the neutral fraction presumably increases by an enormous amount over a very small distance, so both Lyman- α and Lyman- β should become optically thick at nearly the same radius. Unfortunately, this test is still sensitive to the large amount of scatter in the IGM density field (and in the lower-redshift Lyman- α forest that coincides with and hence obscures the Lyman- β measurement), so the current sample of < 10 quasars cannot distinguish these two scenarios – even though coincident Lyman- α and Lyman- β absorbers

have been detected, it is not clear if they are due to a large swath of neutral IGM gas or a single absorber.¹ Simulations suggest that increasing the sample of these spectra by a factor of a few could lead to useful constraints when $\bar{x}_{\text{HI}} > 0.1$, the regime in which the finite bubble size starts to affect the Lyman- β near-zone size.

Another difficulty with near-zone measurements, just as with the classical proximity effect, is the biased region in which the quasar lives. Although the gas is only significantly overdense in a relatively small region immediately around the quasar, even modest overdensities in the dark matter can lead to substantial overdensities in the biased galaxy population. Moreover, the ionized bubble generated by these galaxies reaches much larger distances than the galaxy overdensity itself – even the tens of comoving Mpc typical of a bright quasar’s near-zone. The easiest way to understand this is to think of the overdense region as a piece of a Universe with $\Omega_m > 1$: in that case structure formation proceeds faster, because of the increased gravity, and both the local ionized fraction and the ionized bubbles themselves grow faster as well.

This implies that the ionized fraction measured from the quasar near-zone will be biased relative to the true average.

1.4 THE RED DAMPING WING

However, if such red photons encounter nearly neutral gas, with $\tau_\alpha > 10^5$, its extremely broad absorption line can significantly affect their transfer through the IGM. Considering only the regime in which $|\nu - \nu_\alpha| \gg \Lambda_\alpha$ (and neglecting the broadening introduced by the finite temperature of the IGM), we may ignore the second term in the denominator of equation (??). If we assume that the IGM has a uniform neutral fraction \bar{x}_D at all points between the edge of a source’s local ionized bubble (which we call z_b) and z_{reion} , this leads to an analytical result valid within the “red damping wing” of the Gunn-Peterson trough for the optical depth at an observed wavelength $\lambda_{\text{obs}} = \lambda_\alpha(1+z)$:

$$\tau(z) = \tau_\alpha \bar{x}_D \left(\frac{\Lambda}{4\pi^2 \nu_\alpha} \right) \left(\frac{1+z_b}{1+z} \right)^{3/2} \left[I \left(\frac{1+z_b}{1+z} \right) - I \left(\frac{1+z_{\text{reion}}}{1+z} \right) \right], \quad (1.17)$$

for $z > z_b$, where

$$I(x) \equiv \frac{x^{9/2}}{1-x} + \frac{9}{7}x^{7/2} + \frac{9}{5}x^{5/2} + 3x^{3/2} + 9x^{1/2} - \frac{9}{2} \ln \left[\frac{1+x^{1/2}}{1-x^{1/2}} \right]. \quad (1.18)$$

Note that here we define z as the redshift at which the observed photon would have passed through Lyman- α ; however, when $z > z_b$ this never actually happens. This expression is only valid far from line center, but that is usually acceptable because the optical depth is so large there anyway. It also assumes $\Omega_m(z) = 1$, which is adequate in the high energy limit.

¹These kinds of identifications are further complicated by the damping wing absorption that we will examine next.

For wavelengths for which $|x - 1| \ll 1$ in both factors, one can approximate the $I(x)$ factors with their asymptotic limits; in that case,

$$\tau(z) \approx \tau_\alpha \bar{x}_D \left(\frac{\Lambda}{4\pi^2 \nu_\alpha} \right) (1+z)^2 \left(\frac{1}{z - z_b} - \frac{1}{z - z_{\text{reion}}} \right). \quad (1.19)$$

As a rule of thumb, the damping wing optical depth approaches unity at a velocity offset of $\sim 1500 \text{ km s}^{-1}$, which corresponds to ~ 1 proper Mpc at high redshifts.

The exciting prospect is that, within this red damping wing, the optical depth experienced by the photons approaches order unity over a fairly wide range of redshifts: this means that the optical depth can be measured relatively easily, in contrast to the strongly saturated absorption at line center. Crudely, if we can therefore measure z_s and $\tau(z)$ we can obtain an estimate for the IGM neutral fraction.

Figure 1.4 illustrates the resulting absorption profiles for three choices of $\bar{x}_D = 0.9, 0.5,$ and 0.1 (thin dashed, solid, and dotted curves, respectively); in all cases we take $z_{\text{reion}} \ll z_b$. Here the abscissa measures the wavelength offset from the source redshift z_s ; we take z_b , where neutral gas first appears, to be 5 cMpc from the source. Note that, especially for the more neutral cases, the absorption extends to quite large redshift offsets from line center: $z - z_s = 0.01(1 + z_s)$ translates to an observed wavelength offset of $12(1 + z_s) \text{ \AA}$. The dot-dashed line shows the absorption profile of a single absorbing cloud at a fixed location (i.e., a DLA), normalized to have the same transmission at z_s as the $\bar{x}_D = 0.1$ curve.

Obviously, the IGM absorption profile is much gentler than that from a DLA, extending to much larger redshift offsets. Indeed, equation (1.19) shows that the optical depth goes like the inverse of the wavelength offset between the observed wavelength and λ_α at the source redshift. In contrast, DLAs have $\tau \propto \Delta\lambda^{-2}$; the difference arises because the photon continues to redshift away from line center as it passes through the IGM, so a photon at a given wavelength experienced a larger optical depth than one would expect had it remained at a constant frequency through the entire column. In practice, this may be a crucial discriminant between absorption intrinsic to a high-redshift source (taking the form of a DLA) and that from the IGM. For example, nearly all GRBs at lower redshifts have associated high-column absorbers. The different absorption profiles are crucial for discriminating these clouds.

Unfortunately, the simple toy model we have used so far does not accurately describe the IGM during reionization, and the real absorption profiles are likely to be somewhere between these two limits. We have already seen that in most reionization scenarios the IGM has a two-phase structure, with seas of neutral gas surrounding bubbles of ionized matter. A typical line of sight through the IGM will therefore pass through a ‘‘picket fence’’ of absorbers composed of alternating patches of nearly neutral and nearly ionized gas. The resulting absorption profiles, shown for a toy model by the thick lines in Figure 1.4, are steeper than those in a uniform IGM (unless the ionized bubbles are very rare) but shallower than for a DLA: essentially, the photon passes through a series of DLAs separated by clear regions. Because their frequency still changes as they travel, they experience more absorption than for a single cloud.

Obviously, this introduces some significant complications into interpreting the

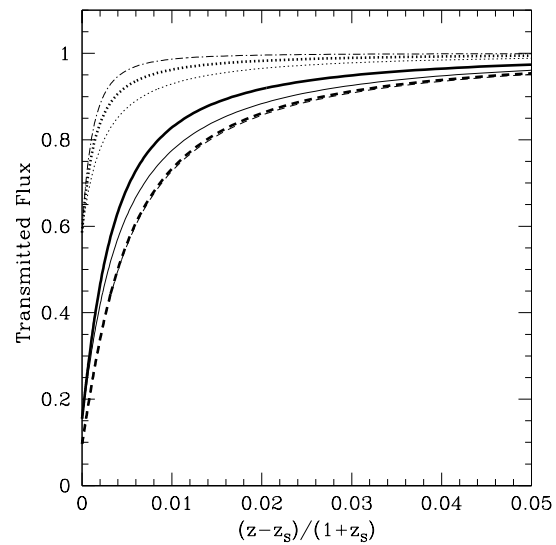


Figure 1.4 Damping wing absorption profiles, as a function of fractional wavelength offset from the source (at redshift z_s). The thick curves show the absorption profiles for $\bar{x}_D = 0.9, 0.5$, and 0.1 assuming our “picket fence” model of absorption (with the dashed, solid, and dotted curves, respectively). Note that the two dashed curves overlap and are practically indistinguishable. The corresponding thin curves show the absorption profiles for uniformly ionized IGM normalized to the same transmission at z_s . The dot-dashed curve shows the profile of a DLA, normalized to the same transmission as the $\bar{x}_D = 0.1$ curves at z_s . Figure credit: Mesinger, A. & Furlanetto, S.R. 2008, MNRAS, 385, 1348.

damping wing. The easiest way to see this is to consider our crude estimate for the average ionized fraction in a uniform IGM, from equation (1.19). Here we can estimate \bar{x}_D from the absorption at a single wavelength, provided that we assume a $1/\Delta\lambda$ profile to be accurate. (Note that we could also estimate z_b from the peak of the absorption line.) In this ‘‘picket fence’’ model, the true optical depth is a sum over that from all the neutral stretches of the IGM, or

$$\tau(z) \approx \tau_\alpha \left(\frac{\Lambda}{4\pi^2\nu_\alpha} \right) (1+z)^2 \sum_i \left(\frac{1}{z-z_{b,i}} - \frac{1}{z-z_{e,i}} \right). \quad (1.20)$$

where the i th neutral patch stretches between $z_{b,i}$ and $z_{e,i}$. If we naively equate this true expression to equation (1.19) and solved for \bar{x}_D , we find

$$\bar{x}_D \approx (z-z_{b,1}) \left\langle \sum_i \left(\frac{1}{z-z_{b,i}} - \frac{1}{z-z_{e,i}} \right) \right\rangle. \quad (1.21)$$

If we take a particularly simple model for the picket fence absorbers, in which the ionized and neutral patches have fixed lengths R_b and fR_b , where $f = (1 - Q_{\text{HII}})/Q_{\text{HII}}$ ensures the proper filling fraction of the bubbles, we can perform this sum and calculate the bias in our estimator $(\bar{x})_D$:

$$\bar{x}_D = \frac{1}{2} \sum_{k=1}^{\infty} \left[\frac{1}{(k-1/2) + (k-1)f} - \frac{1}{(k-1/2) + kf} \right] \quad (1.22)$$

$$= \pi(1 - Q_{\text{HII}}) \cot \left[\frac{\pi(1 - Q_{\text{HII}})}{2} \right]. \quad (1.23)$$

This difference $\bar{x}_D - (1 - Q_{\text{HII}})$ is always positive and peaks at ~ 0.3 when $Q_{\text{HII}} = 0.5$, though the fractional bias continues to increase as $Q_{\text{HII}} \rightarrow 1$. The actual amount of the bias of course depends upon the particular model of reionization (and in particular the size distribution and clustering of the H II regions); more detailed simulations have comparable (though slightly smaller) bias. This means that the damping wing requires non-trivial modeling to interpret it properly in the context of reionization.

Even if this bias can be corrected, a second problem is that different lines of sight inevitably pass through different sets of ionized and neutral patches, so there can be large scatter in the absorption profiles even for a given Q_{HII} and bubble size distribution. This scatter becomes particularly important in the late stages of reionization, because the damping wing optical depth is rather sensitive to the size of the first neutral patch.

Figure 1.5 illustrates these two problems in the context of a more realistic semi-numeric model of reionization. The curves show the probability distribution of $\delta_{x_D} \equiv \bar{x}_D/(1 - Q_{\text{HII}}) - 1$ for a variety of bubble filling factors. Note that the means of these distributions are non-zero (implying a bias in the estimator) and the scatter increases dramatically in the later stages of reionization. This means that reliable estimates of the IGM properties will require a large number of lines of sight with measured damping wings.

Because the damping wing absorption profile must itself be measured, damping wing constraints on reionization require very bright sources. The two most likely

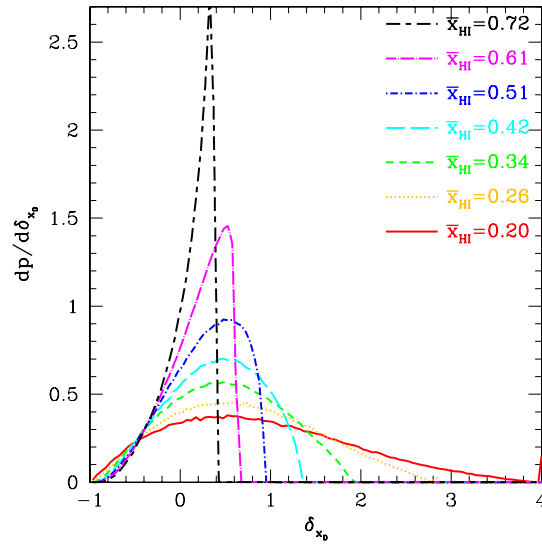


Figure 1.5 Probability distributions of the fractional bias in a simple damping wing estimate of the ionized bubble filling factor, $\delta_{x_D} \equiv \bar{x}_D / (1 - Q_{\text{HII}}) - 1$. The different curves show different stages in reionization; all are computed with a semi-numeric simulation of reionization. Note that the mean is always non-zero, and the distribution becomes both wider and more biased as reionization progresses. Figure credit: Mesinger, A. & Furlanetto, S.R. 2008, MNRAS, 385, 1348.

candidates are quasars and GRBs. The former have the advantage of lying inside large H II regions, which decreases the bias and scatter in the estimators; however, they often also have substantial Lyman- α lines with unknown intrinsic properties, which complicates the measurement of the damping profile. GRBs have much simpler intrinsic spectra (nearly power-law over this range), which makes extracting the damping wing easier. However, their host galaxies often have strong DLA absorbers, which interfere with the damping wing, and their position inside of small galaxies makes the bias and scatter large. It is not clear which will eventually prove more useful, though in either case constructing samples of many objects will be difficult.

1.4.1 Lyman- α Halos Around Distant Sources

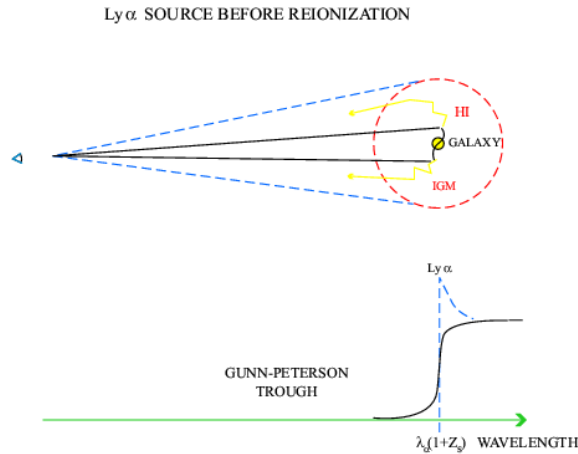


Figure 1.6 Halo of scattered Lyman- α line photons from a galaxy embedded in the neutral IGM prior to reionization (also called a *Loeb-Rybicki halo*). The line photons diffuse in frequency due to the Hubble expansion of the surrounding medium and eventually redshift out of resonance and escape to infinity. A distant observer sees a Lyman- α halo surrounding the source, along with a characteristically asymmetric line profile. The observed line should be broadened and redshifted by about one thousand km s^{-1} relative to other lines (such as H α) emitted by the galaxy.

As we have already discussed in the context of Lyman- α scattering within galaxies, Lyman- α line photons emitted by these galaxies are not destroyed but instead are absorbed and re-emitted as they scatter. For scattering in the uniform IGM, this problem is particularly simple and illuminates more of the physics of the scattering process.

Due to the Hubble expansion of the IGM around the source, the frequency of the photons is slightly shifted by the Doppler effect in each scattering event. As a result, the damping wing photons diffuse in frequency to the red side of the Lyman- α resonance. Eventually, when their net frequency redshift is sufficiently large,

they escape and travel freely towards the observer (see Figure 1.6). As a result, the source creates a faint Lyman- α halo on the sky.ⁱⁱ These *Loeb-Rybicki* Lyman- α halos can be simply characterized by the frequency redshift relative to the line center, $\nu_* = |\nu - \nu_\alpha|$, which is required in order to make the optical depth from the source equal to unity. At high redshifts, the leading term in equation (1.17) yields

$$\nu_* = 8.85 \times 10^{12} \text{ Hz} \times \left(\frac{\Omega_b h}{0.05 \sqrt{\Omega_m}} \right) \left(\frac{1+z_s}{10} \right)^{3/2}, \quad (1.24)$$

as the frequency interval over which the damping wing affects the source spectrum. A frequency shift of $\nu_* = 8.85 \times 10^{12}$ Hz relative to the line center corresponds to a fractional shift of $(\nu_*/\nu_\alpha) = (v/c) = 3.6 \times 10^{-3}$ or a Doppler velocity of $v \sim 10^3 \text{ km s}^{-1}$. The Lyman- α halo size is then defined by the corresponding proper distance from the source at which the Hubble velocity provides a Doppler shift of this magnitude,

$$r_* = 1.1 \left(\frac{\Omega_b/0.05}{\Omega_m/0.3} \right) \text{ Mpc}. \quad (1.25)$$

Typically, the observable Lyman- α halo of a source at $z_s \sim 10$ occupies an angular radius of $\sim 15''$ on the sky (corresponding to $\sim 0.1 r_*$) and yields an asymmetric line profile as shown in Figures 1.6 and 1.7. The scattered photons are highly polarized and so the shape of the halo would be different if viewed through a polarization filter.

Detection of the diffuse Lyman- α halos around bright high-redshift sources (which are sufficiently rare so that their halos do not overlap) would provide a unique tool for probing the distribution and the velocity field of the neutral IGM before the epoch of reionization. The Lyman- α sources serve as lamp posts which illuminate the surrounding H I fog. However, due to their low surface brightness, the detection of Lyman- α halos through a narrow-band filter is much more challenging than direct observation of their sources. Moreover, the velocity fields around these galaxies may be complicated by winds and infall, which would affect the line brightness and profile in similar ways to those discussed in §1.1.1.

1.5 THE Lyman- α FOREST AS A PROBE OF THE REIONIZATION TOPOLOGY?

Given the enormous utility of the Lyman- α forest for understanding the ionization state of the IGM at low and moderate redshifts, extension of these techniques to the cosmic dawn is an obvious test of the topology and nature of the reionization process. However, we have already seen that the Gunn-Peterson optical depth is enormous at this time, even in highly ionized gas. Thus we should not expect a clear signature of the ionized bubbles.

ⁱⁱThe photons that begin blueward of Lyman- α and are absorbed in the Gunn-Peterson trough are also re-emitted by the IGM around the source. However, since these photons originate on the blue side of the Lyman- α resonance, they travel a longer distance from the source, compared to the Lyman- α line photons, before they escape to the observer. The Gunn-Peterson photons are therefore scattered from a larger and hence dimmer halo around the source.

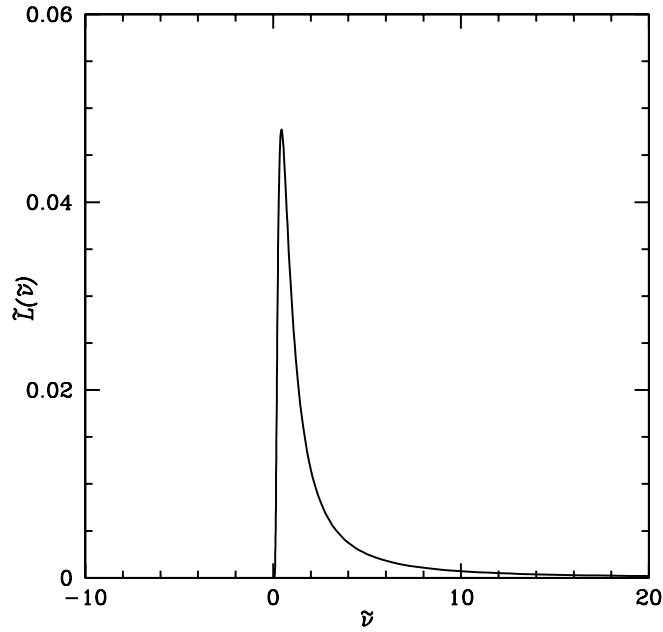


Figure 1.7 Monochromatic photon luminosity of a Lyman- α halo as a function of normalized frequency shift from the Lyman- α resonance, $\tilde{\nu} \equiv (\nu_\alpha - \nu)/\nu_*$. Note that only the photons inside the red damping wing scatter in this compact halo; those on the blue side of Lyman- α scatter at much larger distances. The observed spectral flux of photons $F(\nu)$ (in photons $\text{cm}^{-2} \text{s}^{-1} \text{Hz}^{-1}$) from the entire Lyman- α halo is $F(\nu) = (\tilde{L}(\tilde{\nu})/4\pi d_L^2)(\dot{N}_\alpha/\nu_*)(1+z_s)^2$ where \dot{N}_α is the production rate of Lyman- α photons by the source (in photons s^{-1}), $\nu = \tilde{\nu}\nu_*/(1+z_s)$, and d_L is the luminosity distance to the source. Figure credit: Loeb, A. & Rybicki, G. B. *Astrophys. J.* **524**, 527 (1999); see also **520**, L79 (1999)].

Nevertheless, the nature of the transformation from a bubble-dominated IGM to the post-reionization “web-dominated” IGM does offer some hope. Once the ionized bubbles become larger than the mean free path of the ionizing photons, the ionizing background saturates – even if the Universe were fully-ionized, the metagalactic background would not increase. Thus, in bubbles that have reached this saturation limit, we can expect (nearly) as much transmission as in the post-reionization IGM.

The key difference is the presence of the damping wing from the neutral gas surrounding each ionized bubble. With the rule of thumb that $\tau_d < 1$ only at distances > 1 proper Mpc from fully neutral gas, this requires that ionized bubbles be at least a few proper Mpc large in order to allow for any transmission. Fortunately, in most reionization models this constraint is easily fulfilled, at least in the latter half of reionization (see Fig. ??, for example).

On the other hand, even a moderate damping wing optical depth still increases the required transmission allowed by the residual neutral gas inside the bubble. Because bubbles that allow transmission must be very large, and thus contain an enormous number of luminous sources, their ionizing background is quite uniform (except at the edges of the bubble, but there the damping wing is large anyway). Thus, just as in the post-reionization IGM, transmission will come from highly-underdense voids in which the neutral fraction is small. Equation (1.11) shows that $\tau < 1$ requires $\delta < 0.1$ – 0.2 . Such deep voids are very rare at high redshifts, because structure formation is still in its infancy – and of course such regions are largely empty of galaxies and so are likely to remain neutral throughout nearly all of reionization.

Thus we expect transmission spikes to be extremely rare during reionization, but not completely impossible. With models for the H II region sizes, the emissivity of the galaxies driving reionization, and of the density distribution of the IGM, it is not hard to estimate the possible abundance of transmission features. Figure 1.8 shows an optimistic example calculation for transmission at $z = 6.1$ (in the range probed by the highest-redshift known quasars). In this case, the IGM density distribution is calibrated to numerical simulations at $z = 2$ – 4 . The curves show that observable transmission gaps, with $\tau < 2.3$ occur only about once per $\Delta z \sim 3$.

In reality, transmission will be even more rare because this simple calculation makes the optimistic assumption that photons travel to the edge of their bubble, without any limits from LLSs in the IGM. But even so, Figure 1.8 shows that they are sufficiently rare that precise quantitative constraints on reionization from the gaps will require much larger samples of quasars or GRBs than currently available. Drawing conclusions about reionization from the forest is instead very difficult. Indeed, some simulations of the reionization process show that the present data cannot even rule out reionization ending at $z < 6$, since some small pockets of neutral gas could remain, buried inside the long stretches of saturated absorption that are common at this time.

Instead, the Lyman- α forest (especially together with absorption in Lyman- β and Lyman- γ) is best at constraining the very end of the reionization era, as discussed in §??, unless the red damping wing can be measured on its own.

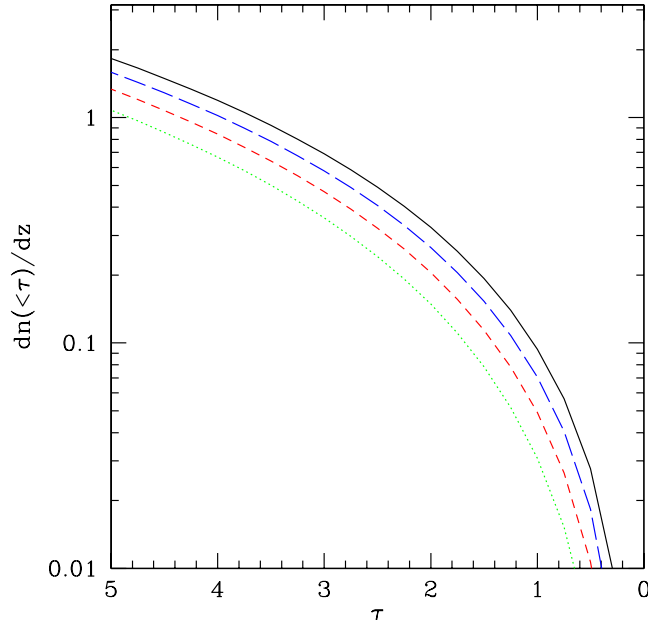


Figure 1.8 A model for the expected cumulative number of transmission features at $z = 6.1$ if the IGM has $Q_{\text{HII}} = 0.9, 0.85, 0.8,$ and 0.75 (solid, long-dashed, short-dashed, and dotted curves, respectively). The model uses the excursion set model for reionization (see §??) and an inhomogeneous IGM density distribution calibrated to simulations at lower redshifts. Figure credit: Furlanetto, S.R. et al. 2004, MNRAS, 354, 695.

1.6 LYMAN- α EMITTERS DURING THE REIONIZATION ERA

We now return to discuss the properties of more normal galaxies that have Lyman- α lines, commonly referred to as Lyman- α emitters or LAEs. We saw in §?? that this strong emission line provides a convenient marker for young star-forming galaxies, and one of the most efficient ways to find distant galaxies is with narrowband searches that identify sources with strong emission lines in a narrow redshift range.

We have seen in §1.1.1 that the intrinsic properties of these lines depend on a host of complex factors. However, we have also seen in §1.3.1 and 1.4 that resonant absorption in the ionized IGM and much stronger absorption from neutral gas – even from the damping wing once the photon has passed through resonance – can also strongly affect the line. These latter effects make the Lyman- α emission lines of galaxies an interesting and potentially powerful probe of IGM properties. However, we must always bear in mind the complexity of the intrinsic lines as an important source of systematic confusion for such a probe.

Figure 1.9 shows how this IGM reprocessing can dramatically alter the observed line intensity and profile; the top panel shows the lines, while the bottom panel

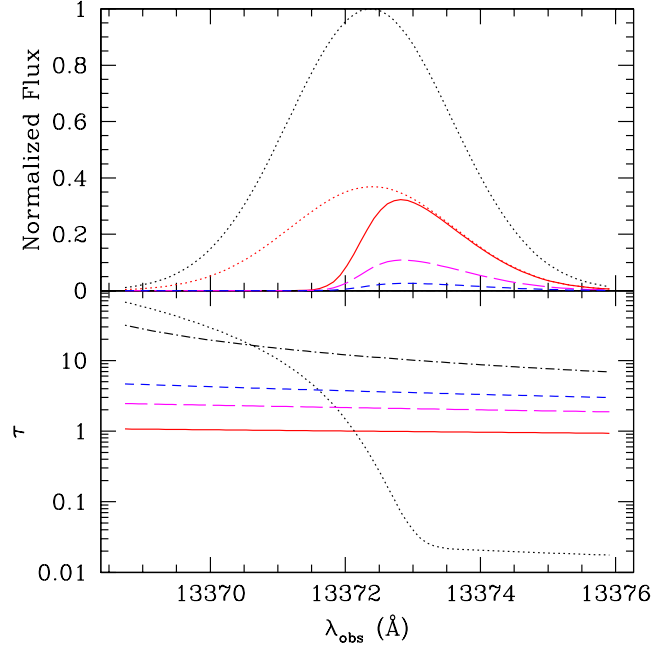


Figure 1.9 *Top*: Example line profiles for a galaxy at $z = 10$. The upper dotted curve shows the intrinsic line profile, assumed to be a gaussian with standard deviation 27 km s^{-1} . The solid, long-dashed, and short-dashed curves show the observed line after reprocessing through the IGM; they place the galaxy in ionized bubbles with radii $R_b = 10, 5,$ and 3 comoving Mpc, respectively. The lower dotted curve shows the line if we neglect resonant absorption within the ionized bubble, assuming $R_b = 10$ Mpc. *Bottom*: The dotted line shows the resonant absorption from the ionized bubble. The solid, long-dashed, short-dashed, and dot-dashed curves show the damping wing optical depth for $R_b = 10, 5, 3,$ and 1 Mpc, respectively. Figure credit: Furlanetto, S.R. et al. 2004, MNRAS, 354, 695.

shows the corresponding optical depth profiles. In the top panel, the upper dotted curve shows the assumed intrinsic line, which we place at $z = 10$ and take as a gaussian with width 27 km s^{-1} (these are arbitrary choices chosen for illustrative purposes). The other curves show the effects of IGM reprocessing, including both the damping wing from fully neutral gas at a distance R_b from the line source (with R_b decreasing from top to bottom) and resonant scattering from the ionized medium within (except for the lower dotted curve). The optical depths providing this absorption are shown in the bottom panel: the nearly-horizontal lines are the damping wing optical depths (with R_b increasing from bottom to top), while the dotted curve shows the resonant value.

Note that the resonant absorption is large everywhere blueward of line center, but it is modest or negligible on the red side. This is a rather generic result (here we have included only the ionization from the galaxy itself, which dominates on the

relevant scales, so the ionization structure on large scales is negligible); in general we expect LAEs at $z > 5$ to have asymmetric line profiles, with the blue side cut off by resonant IGM absorption.

However, the damping wing absorption that affects the red side (as well as the blue side) depends sensitively on the large scale environment, and in particular the displacement from the source to the nearest neutral gas. We see here that a bubble with $R_b = 1$ proper Mpc provides $\tau_D \approx 1$; in fact this rule of thumb works reasonably well throughout the relevant high- z regime.

We therefore expect that, as we penetrate farther back into the reionization era, with the bubbles growing smaller and smaller, more and more of their Lyman- α lines will be extinguished by the neutral gas. In the remainder of this section we will explore the consequences of this expectation for LAE surveys during reionization.

1.6.1 Galaxies within Ionized Bubbles

In order to understand the interplay between the damping wing and galaxy populations, we must first understand how galaxies populate the H II regions that surround them. Fortunately, because we can use the same methods – the excursion set formalism – to compute the halo and ionized bubble abundances, this is a relatively easy task.

Consider an ionized bubble with mass m_b and a mean overdensity δ_b ; according to the model in §??, this overdensity is exactly that required for a collapse fraction large enough to produce one ionizing photon per hydrogen atom inside the bubble, so $\delta_b = B(m_b)$. We wish to know the abundance of galaxies as a function of mass m within this ionized bubble, $n(m|m_b)$.

In the excursion set picture (see §??), this is simply proportional to the fraction of random walks that begin at (m_b, δ_b) and end at (m, δ_c) , where δ_{crit} is the critical linearized overdensity for halo collapse (which is a function of m in, for example, the Sheth-Tormen model). But this problem is actually identical to the “extended Press-Schechter” problem, in which we calculated the progenitors of a given halo at an earlier redshift: the only difference is that here our “halo” is a bubble and we work at the same redshift – which is possible because the criterion for an ionized bubble requires a lower overdensity than halo collapse itself.

Thus we can immediately write

$$n(m|m_b) = \sqrt{\frac{2}{\pi}} \frac{\bar{\rho}}{m^2} \left| \frac{d \ln \sigma}{d \ln m} \right| \frac{\sigma^2 [\delta_{\text{crit}}(z) - B(m_b)]}{(\sigma^2 - \sigma_b^2)^{3/2}} \exp \left\{ -\frac{[\delta_{\text{crit}}(z) - B(m_b)]^2}{2[\sigma^2 - \sigma_b^2]} \right\}, \quad (1.26)$$

where $\sigma^2 = \sigma^2(m)$ and $\sigma_b^2 = \sigma^2(m_b)$.

We can also perform the reverse calculation (analogous to the distribution of halo descendants) to compute the probability $p_b(m_b|m)$ that a halo of mass m is part of a bubble of mass m_b . Figure 1.10 shows the results of this calculation for a small halo ($m_h = 10^9 M_\odot$) and a moderately large one ($m_h = 10^{11} M_\odot$). The different curves in each panel correspond to a sequence of ionized fractions in a model of reionization. Unsurprisingly, the median bubble size increases as reionization progresses (because all bubbles grow with time), but note that it also strongly depends on the halo mass: large galaxies are far more likely to reside

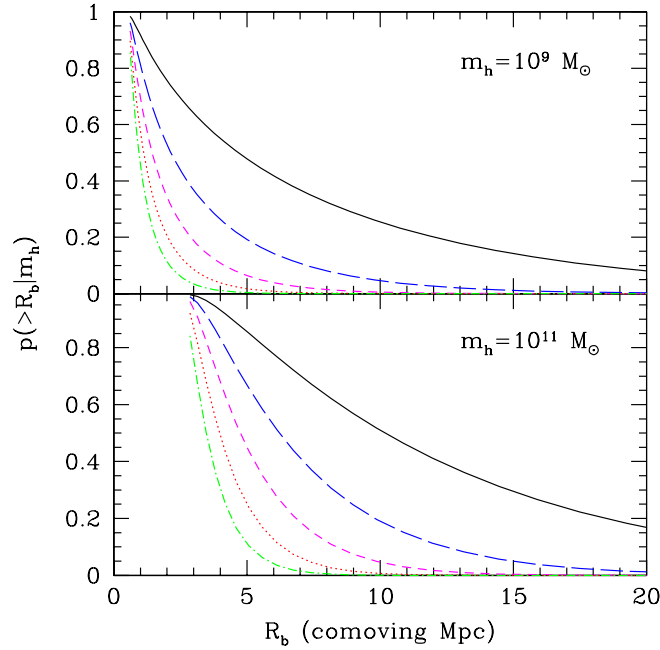


Figure 1.10 Probability that halos with $m_h = 10^9$ and $10^{11} M_\odot$ reside in ionized bubbles larger than a given radius R_b . Here we use the excursion set model of reionization with $\zeta = 40$; the bubble sizes are relatively independent of this choice, for a fixed Q_{HII} , but the halo populations themselves are highly-redshift dependent. In each panel, the curves correspond to $z = 12$ ($Q_{\text{HII}} = 0.74$, solid), $z = 13$ ($Q_{\text{HII}} = 0.48$, long dashed), $z = 14$ ($Q_{\text{HII}} = 0.3$, short-dashed), $z = 15$ ($Q_{\text{HII}} = 0.19$, dotted), $z = 16$ ($Q_{\text{HII}} = 0.11$, dot-dashed), Figure credit: Furlanetto, S.R. et al. 2004, MNRAS, 354, 695.

in large bubbles than average galaxies. This is just another manifestation of the increasing bias of galaxies with their mass.

1.6.2 LAE Number Counts During Reionization

Now let us consider the following experiment. We imagine performing a sequence of narrowband Lyman- α searches at progressively larger redshifts. We expect that, once the typical bubble size falls below ~ 1 proper Mpc, the IGM damping wing will also start to extinguish the lines even if the galaxies still exist. We might therefore imagine a simple counting exercise as a test for reionization, aiming to see a decline in the abundance of LAEs.

Of course, there are many other reasons why the LAE density may decline – most obviously, the halo mass function changes rapidly with z at these early times, so the galaxy abundance most likely does as well. Ideally one would therefore calibrate it to a broadband galaxy survey that is not subject to the same selection effects – if

the LAE abundance declines precipitously while the overall galaxy density declines only gently, that would be good evidence for IGM absorption. Note, however, that the complicated physics of Lyman- α generation and transfer within galaxies always leaves some room for doubt, since such a decline could also be attributed to the evolving IMF of stars or changes in their dust content.

Nevertheless, this simple test is very attractive. We can use the excursion set formalism described in §1.6.1 to estimate how the abundance would decline. We ignore the effects of resonant absorption (since they depend on the local environment of the galaxy and hence are unlikely to evolve rapidly during reionization) but include the damping wing absorption from neutral gas in the IGM. Let us suppose that the survey is sensitive to sources with $L > L_{\min}$. If we then take $L \propto m$ for simplicity, a galaxy of mass m will be detected only if the damping wing has $\tau_D < \ln(m/m_{\min})$, where $L(m_{\min}) = L_{\min}$. Then the number density of observable galaxies is

$$n(> L) = \int dm_b n_b(m_b) V_b \int_{m_D}^{\infty} dm n(m|m_b), \quad (1.27)$$

where m_D is the minimum halo mass that remains observable inside a bubble of mass m_b and volume V_b ; note that it *decreases* with m_b , since larger bubbles cause less damping wing absorption. Of course, in reality τ_D is a function not only of bubble size but of a galaxy's position within the bubble: those at the edge always experience strong absorption.

Nevertheless, this simple model is in good agreement with more detailed calculations using simulations of reionization (either full-scale or semi-numeric). Figure 1.11 shows the luminosity function at several different neutral fractions (including fully ionized, top curve) measured in a semi-numeric simulation. Clearly damping wing absorption from the neutral gas can have an enormous effect on the observed abundance of galaxies in these surveys.

The detailed calculation reveals two interesting effects. First, the fractional decline is relatively modest (no more than a factor ~ 2) until $Q_{\text{HII}} < 0.5$; after that point the abundance declines precipitously. This is because the ionized bubbles have characteristic sizes ~ 10 comoving Mpc, or ~ 1 proper Mpc, at about filling factor. Larger bubbles, late in reionization, have $\tau_D < 1$ and so have only a small effect on the observed abundance.

The second factor is visible in the bottom panel of Figure 1.11: evidently the fractional decline in LAE abundance is nearly independent of halo mass (or intrinsic luminosity). This occurs because the distribution of τ_D is quite broad (roughly lognormal), thanks not only to the range of halo sizes but also to the distribution of galaxies within each bubble. For faint galaxies, which roughly follow a power-law intrinsic distribution, the convolution of these two effects preserves the power law. At the bright end, where the intrinsic luminosity function declines exponentially, the breadth of the τ_D distribution masks the change in slope.

Despite many surveys at $z < 6.6$ and a few detections of LAEs at $z > 7$, there is currently no strong evidence for any substantial decline in their number counts relative to galaxies selected with other techniques. This is not particularly surprising, given that the effects do not become dramatic until $Q_{\text{HII}} < 0.5$. But this promises

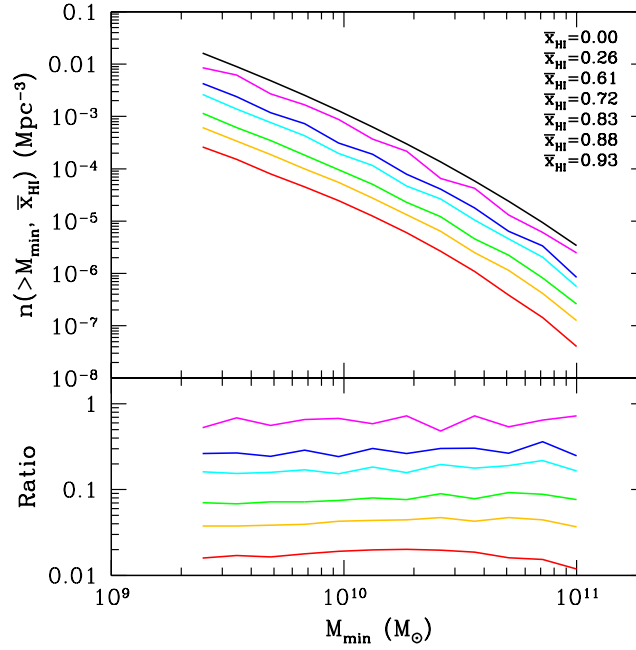


Figure 1.11 Luminosity function of LAEs at $z = 9$ in a semi-numeric simulation of reionization, as a function of the mean neutral fraction \bar{x}_{HI} . The sequence of curves from top to bottom goes from small to large \bar{x}_{HI} . The bottom panel shows the ratio of the curves to that in a fully-ionized Universe. Figure credit: Mesinger, A. & Furlanetto, S.R. et al. 2008, MNRAS, 386, 1990.

to be a much more powerful technique with the more efficient high-redshift galaxy studies enabled by JWST and other forthcoming telescopes.

1.6.3 LAE Clustering During Reionization

The fact that galaxies within large ionized bubbles remain (relatively) unattenuated while those inside of small bubbles will be extinguished by the damping wing suggests that not just the mean number density of LAEs will change throughout reionization, but that their spatial distribution will evolve as well. Figure 1.12 shows this explicitly. Each panel shows a slice through a semi-numeric simulation of reionization; here we fix $z = 9$ and vary the ionized fraction across the panels (from fully-ionized at left to $\bar{x}_{\text{HI}} = 0.77$ at right). Each white dot corresponds to a galaxy with an observable Lyman- α line, assuming the same model as the last section for their luminosity function. The overall trend is clear: galaxies that are relatively isolated in the left-most panel disappear first, while those that are part of a strong overdensity (near the bottom center of the image) remain visible even to large neutral fractions.

The best way to describe this phenomenon quantitatively is through the cluster-

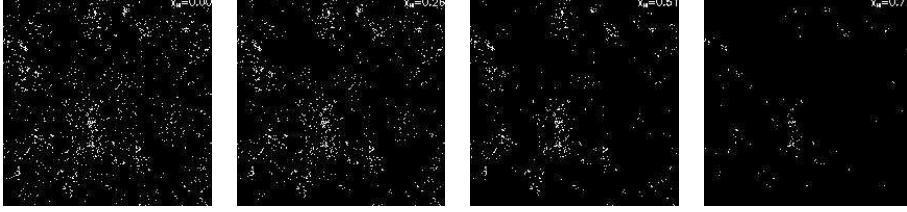


Figure 1.12 Maps of visible LAEs at $z = 9$ in a semi-numeric simulation, assuming $\bar{x}_{\text{HI}} \approx 0, 0.26, 0.51, 0.77$, from left to right. All slices are 250 Mpc on a side and 20 Mpc deep. We assume that all halos with observed luminosities greater than that corresponding to an unattenuated galaxy with $M > 1.67 \times 10^{10} M_{\odot}$ are visible. Figure credit: Mesinger, A. & Furlanetto, S.R. et al. 2008, MNRAS, 386, 1990.

ing of the galaxies. A simple toy model illustrates how it enhances the apparent clustering on small scales (relative to galaxies observed in the continuum, for example). Suppose that galaxies with number density \bar{n} are distributed randomly throughout the universe but that we can only observe those with at least one neighbor within a sphere of volume $V \ll \bar{n}^{-1}$. Assuming a Poisson distribution, the number density of observed objects would be

$$n_{\text{obs}} = \bar{n}(1 - e^{-\bar{n}V}). \quad (1.28)$$

As usual the correlation function of the observed sample is defined through the total probability of finding two galaxies in volumes δV_1 and δV_2 ,

$$\delta P = n_{\text{obs}}^2 (1 + \xi) \delta V_1 \delta V_2. \quad (1.29)$$

However, we know that every observed galaxy has a neighbour within V ; thus

$$\delta P = n_{\text{obs}} \delta V_1 (\delta V_2/V) \quad (1.30)$$

for small separations (where the factor $\delta V_2/V$ assumes the neighbor to be randomly located within V). Thus,

$$\xi = 1/(n_{\text{obs}}V) - 1 \quad (1.31)$$

on such scales: even though the underlying distribution is random, the selection criterion induces clustering. Note that it can be extremely large if $V \ll n_{\text{obs}}^{-1}$.

On large scales, the modulation takes a different form. An observed galaxy resides in a large bubble, corresponding to an overdense region. Because of the bias of the underlying dark matter field, that overdense region will tend to lie near to other overdense regions – and hence to other large bubbles. Thus, we will be more likely to see galaxies near the original object than in an average slice of the universe. Because we do not see similar galaxies in small (less-biased) bubbles, the large-scale bias will generically be larger than that intrinsic to the galaxies.

Because these two effects have different amplitudes, the bubbles introduce a scale-dependent bias to the correlation function of galaxies, with a break at $r \approx R_c$, where R_c is the characteristic size of the ionized bubbles. Again using the excursion set formalism, we can estimate this modified bias in the limits $r \ll R_c$ and $r \gg R_c$.

By analogy with the halo model for the density field, these limiting regimes correspond to correlations between galaxies within a single bubble and within two separate bubbles. We begin with large scales: the observed clustering is the average bias of the bubbles weighted by the number of galaxies in each H II region (analogous to the two-halo term for the density field):

$$b_{r=\infty} = \int dm_b n_b(m_b) b_b(m_b) V_b \int_{m_D}^{\infty} dm_h \frac{n_h(m_h|m_b)}{\bar{n}_{\text{gal}}}, \quad (1.32)$$

where we integrate only over those haloes visible after damping wing absorption and \bar{n}_{gal} is the mean number density of observable galaxies. Following the procedure outlined in §??, we can estimate the bias b_b of H II regions asⁱⁱⁱ

$$b_b(m_b) = 1 + \frac{B(m_b)/\sigma^2(m_b) - 1/B_0(m_b)}{D(z)}. \quad (1.33)$$

(Note that (unlike the halo bias) we can have $b_b < 0$: late in reionization, small bubbles are truly *anti*-biased because dense regions have already been incorporated into large ionized regions.)

The behavior on small scales is somewhat more subtle. If galaxies were randomly distributed within each bubble, the simple argument in the first paragraph of this section suggests that the correlation function would just be the weighted average of the number of pairs per H II region. However, in addition to the increase in the number of galaxies in each bubble, the galaxies also trace density fluctuations within each bubble. On moderately small scales where nonlinear evolution in the density field may be neglected, we therefore write

$$b_{\text{sm}}^2 = \int dm_b n_b(m_b) V_b b_h^2(m_b) \frac{\langle N_{\text{gal}}(N_{\text{gal}} - 1)|m_b \rangle}{\bar{N}_{\text{gal}}^2}, \quad (1.34)$$

where $\bar{N}_{\text{gal}} = \bar{n}_{\text{gal}} V_b$, $\langle N_{\text{gal}}(N_{\text{gal}} - 1)|m_b \rangle$ is the expected number of galaxy pairs within each bubble, and b_h^2 measures the excess bias of these haloes inside each bubble. Note the similarity to the halo-model calculation of the galaxy power spectrum here; in fact this form can be derived formally by constructing the galaxy density field from bubbles and their constituent haloes, in analogy to the halo model. This term then corresponds to the “two-halo, one-bubble” term in such a treatment; i.e., correlations between two particles that lie in the same bubble but different dark matter haloes. The “bubble profile” describing the distribution of galaxies within the bubble turns out to be proportional to the square root of the linear matter correlation function. Provided that the typical bubbles have more than two galaxies, we can write the expected number of pairs as

$$\langle N_{\text{gal}}(N_{\text{gal}} - 1)|m_b \rangle \approx \max\{0, \bar{N}_{\text{gal}}(m_b)[\bar{N}_{\text{gal}}(m_b) - 1]\}. \quad (1.35)$$

The remaining factor is $b_h(m_b)$. It may seem reasonable to take this to be the mean value of the usual excursion set halo bias, evaluated over $n(m_h|m_b)$. However, the pair density inside each bubble *already* includes much of this bias because

ⁱⁱⁱThis equation does not work late in reionization, because the physical requirement that $Q_{\text{HII}} \leq 1$ caps the effective number density and hence the bias. In this regime numerical simulations are necessary; fortunately this regime is also the least interesting from the viewpoint of clustering.

it counts the number of galaxies in a region with overdensity $\delta_b = B$. We therefore only want the “excess” bias of the galaxies relative to density fluctuations on scales smaller than m_b , which is the bias evaluated from the conditional mass function in equation (1.26). Following the excursion set definition of this bias, we have

$$b_h(m_h|m_b) = 1 + \frac{(\delta_c - \delta_x)^2 / (\sigma^2 - \sigma_b^2) - 1}{\delta_c(z=0) - \delta_x(z=0)}. \quad (1.36)$$

We show the resulting bias at $z = 10$ (as a function of Q_{HII}) in Figure ???. In each panel, the different curves take different galaxy populations, with smaller galaxies having less net bias. Panels (a) and (b) show b_{sm} and $b_{r=\infty}$. We scale the results to the bias \bar{b}_h intrinsic to the galaxy population if absorption could be ignored. Panel (c) shows the ratio $b_{r=\infty}/b_{\text{sm}}$, illustrating the magnitude of the “break” in the linear bias. We emphasize that the scale at which the break occurs will evolve throughout reionization along with the characteristic bubble size R_c ; for illustrative purposes we mark several values of R_c .

Clearly, both b_{sm} and $b_{r=\infty}$ decrease throughout reionization. The large-scale bias decreases because the ionized regions must lie nearer to the mean density (and hence be less biased) as $Q_{\text{HII}} \rightarrow 1$: this behaviour must be generic to any model in which reionization begins in overdense regions. The small-scale bias decreases because bubbles large enough to allow transmission become common: early on, only those galaxies with near neighbors are visible, so the correlations are strong. In the middle and final stages of reionization, most galaxies lie inside bubbles large enough to permit transmission, so more typical galaxies become visible and $b_{\text{sm}} \rightarrow \bar{b}_h$.

These qualitative results also hold true in more detailed calculations with numerical simulations. Figure 1.14 shows the estimated angular correlation function (i.e., the three-dimensional correlation function projected on the plane of the sky) from a radiative transfer simulation of LAEs at $z = 6.6$, the highest redshift window easily visible from the ground. The different curves in each panel correspond to different ionized fractions; the different panels describe different surveys, with the top panel comparable to existing capabilities and the others a few times larger. Note the enhancement in small scale correlations at small ionized fractions; this is the same effect we have described with b_{sm} . The large-scale power is also enhanced, but it is much less sensitive to \bar{x}_i .

Although the correlation function and power spectrum (and through them the linear bias) are the most straightforward manifestations of the increased clustering, the “mask” applied to the galaxy distribution is itself non-gaussian, so other clustering statistics – such as counts-in-cells or higher-order correlations – are also useful. All of these probes follow the qualitative behavior of the bias, increasing most dramatically early in the reionization process.

Both the analytic and numeric approaches show that the bias increases by a large factor, at least doubling and sometimes increasing by an even larger amount, especially on large scales. This, together with the change in the shape of the LAE correlation function with respect to the dark matter, makes the clustering signature much more robust to uncertainties in the nature of the LAE hosts. This is because the linear bias is a relatively slowly-varying function of halo mass and redshift;

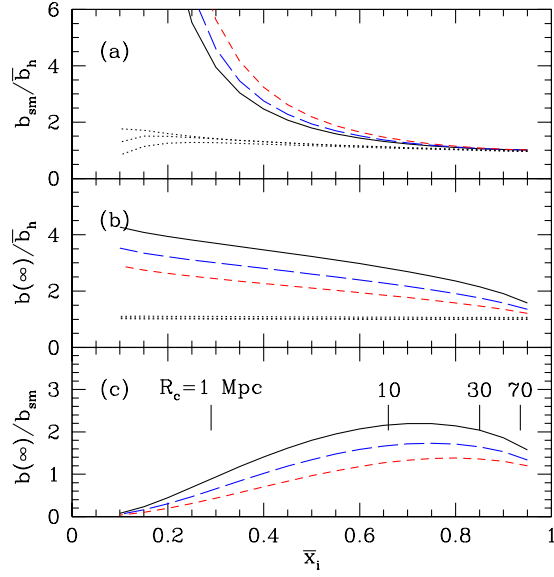


Figure 1.13 (a): Predicted small-scale bias at $z = 10$, relative to the bias expected if all galaxies above the mass threshold were visible. This applies to separations larger than the nonlinear scale but smaller than the characteristic bubble size R_c . The solid, long-dashed, and short-dashed curves take $m_{\text{obs,min}} = 10^8, 10^9$, and $10^{10} M_\odot$, respectively. The dotted curves show the predicted galaxy bias, neglecting absorption, relative to its true value (the small errors at early times result from the approximations described in the text). (b): Predicted large-scale bias at $z = 10$, relative to the bias expected if all galaxies above the mass threshold were visible. (c): Ratio of large to small scale bias; the transition between the two regimes will occur roughly at R_c , which is marked for a few different values of the ionized fraction \bar{x}_i . Figure credit: Furlanetto, S.R. et al. 2006, MNRAS, 365, 1012.

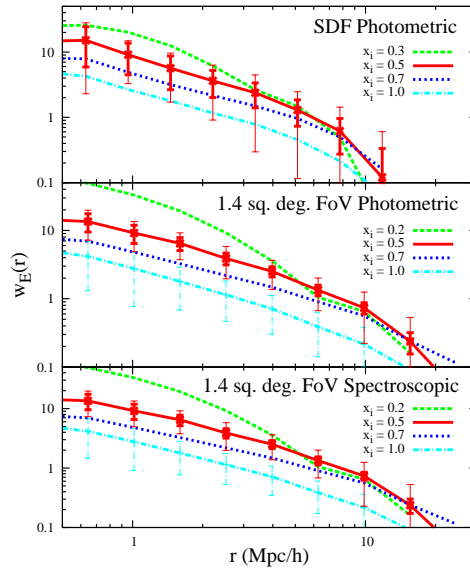


Figure 1.14 Angular correlation function of LAEs in a radiative transfer simulation of reionization. The simulation takes $z = 6.6$ and assumes all LAEs with an observed luminosity greater than the intrinsic luminosity of a halo with $m = 7 \times 10^{10} M_{\odot}$ are visible. The different curves in each panel assume different ionized fractions. The top panel estimates the errors for existing surveys with the Subaru Deep Field in which LAEs are detected photometrically. The other two panels assume larger surveys (with ~ 5 times more LAEs); the middle panel assumes a photometric survey, while the bottom one assumes the LAEs can be selected spectroscopically. In each one, the thick error bars include Poisson fluctuations in the galaxy counts, while the thin curves also include cosmic variance. Figure credit: McQuinn, M. et al. 2007, MNRAS, 381, 75.

mimicking the shift due to reionization would require a drastic change in the properties of the galaxies.

However, it is worth emphasizing again that the radiative transfer of Lyman- α photons through the IGM is a complex process, and it can affect the observed clustering even after reionization is complete (thus the resonant absorption, which we have neglected in this section, can also be important). Interestingly, the frequency dependence of the scattering process induces anisotropies, generating clustering signatures analogous to redshift-space distortions. Fortunately, this component should not evolve as rapidly during reionization as the damping wing.

1.6.4 Lyman- α Blobs

A particularly interesting example of Lyman- α line emission in the interface between galaxies and the IGM are the so-called “Lyman- α blobs” (LABs) originally discovered in narrowband images at moderate redshifts ($z \sim 3$). Since their initial discovery in the year 2000,² several tens of LABs have been found³ in the redshift range $z \sim 2-7$, making them much more common than initially expected. These blobs have a range of properties, but all are characterized by significantly extended Lyman- α line emission (ranging in size from ~ 10 kpc “halos” around star-forming galaxies to > 150 kpc giants with no obvious central galaxy in the rest-frame ultraviolet). Some appear to be diffuse elliptical objects, while others are much more filamentary. The brighter objects, with line luminosities $L > 10^{44} \text{erg s}^{-1}$, are extraordinarily powerful, corresponding to star formation rates $> 50 M_{\odot} \text{yr}^{-1}$. The lines can be quite broad but do not show any unusual features like double-peaked profiles. Two example objects are shown in Figure ??.

Bright LABs are typically located near massive galaxies that reside in dense regions of the Universe. Multi-wavelength studies of LABs reveal a clear association of the brighter blobs with sub-millimeter and infrared sources which form stars at exceptional rates⁴ of $\sim 10^3 M_{\odot} \text{yr}^{-1}$, or with obscured active galactic nuclei (in fact, strong Lyman- α emission has been known for many years to surround some high-redshift radio galaxies).⁵ However, other blobs have been found that are not associated with any source powerful enough to explain the observed Lyman- α luminosities.⁶

The origin of LABs is still unclear. Some models relate LABs to cooling radiation from gas assembling into the cores of galaxies.⁷ Other models invoke photoionization of cold ($T \sim 10^4$ K), dense, spatially extended gas by an obscured AGN⁸ or extended X-ray emission;⁹ the compression of ambient gas by superwinds to a dense Lyman- α emitting shell;¹⁰ or star formation triggered by relativistic jets from AGN.¹¹ The latest models¹² relate LABs to filamentary flows of cold ($\sim 10^4$ K) gas into galaxies, which are generically found in numerical simulations of galaxy formation.¹³ These cold flows contain $\sim 5-15\%$ of the total gas content¹⁴ in halos as massive as $M_{\text{halo}} \sim 10^{12}-10^{13} M_{\odot}$.

Although these objects have only been observed in detail so far at low redshifts, similar mechanisms offer the prospect of learning not only about star formation inside of high-redshift galaxies and the gross properties of the IGM but also about the detailed structure of the gas accreting onto, or flowing out of, young galaxies.

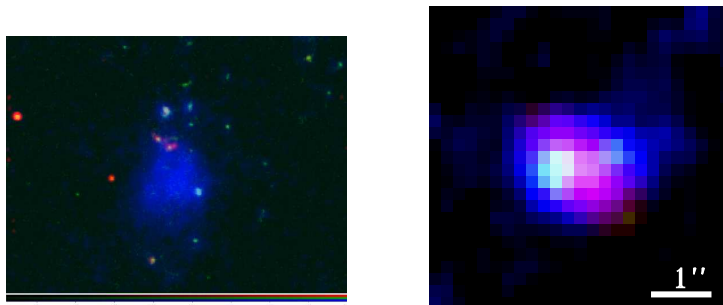


Figure 1.15 *Left:* A false color image of a Lyman- α blob (LAB) at a redshift $z = 2.656$. The hydrogen Lyman- α emission is shown in blue, and images in the optical V-band and the near-infrared J and H bands are shown in green and red, respectively. Note the compact galaxies lying near the northern (top) end of the LAB. The Lyman- α image was obtained using the SuprimeCam imaging camera on the Subaru Telescope, and the V, J, and H band images were obtained using the ACS and NICMOS cameras on the Hubble Space Telescope. This LAB was originally discovered by the Spitzer Space Telescope. Image credit: Prescott, M., & Dey, A. (2010). *Bottom:* A false color image of an LAB at a redshift $z = 6.6$, obtained from a combination of images at different infrared wavelengths. Image credit: Ouchi, M. et al. *Astrophys. J.* **696**, 1164 (2009).

Lyman- α studies may therefore ultimately hold the key to understanding the initial stages of galaxy formation and accretion.